Optical coherence and beamspread in ultrafast-laser pulsetrain-burst hole drilling

Jesse Dean[a], Paul Forrester[a], Martin Bercx[a], David Graper[a],
Luke McKinney[a], Felix Frank[a,c], Marc Nantel[a,b], Robin Marjoribanks[a]

[a]Department of Physics and Institute for Optical Sciences, University of Toronto
60 St George St., Toronto, ON M5S-1A7, Canada

[b]Centre for Photonics, Ontario Centres of Excellence, Inc.
156 Front Street West, Suite 200, Toronto, Ontario M5J 2L6

ABSTRACT

Pulsetrain-burst machining has been shown to have advantages over single-pulse laser processing of materials and biological tissues. Ultrafast lasers are often able to drill holes in brittle and other difficult materials without cracking or swelling the target material, as is sometimes the case for nanosecond-pulse ablation; further, pulsetrain-bursts of ultrafast pulses are able to recondition the material during processing for instance, making brittle materials more ductile and striking advantages can result. In the work we report, we have investigated hole-drilling characteristics in metal and glass, using a Nd:glass pulsetrain-burst laser (1054 nm) delivering $1-10$ ps pulses at 133 MHz, with trains $3-15$ μs long. We show that as the beam propagates down the channel being drilled, the beam loses transverse coherence, and that this affects the etch-rate and characteristics of channel-shape: as the original Gaussian beam travels into the channel, new boundary conditions are imposed on the propagating beam principally the boundary conditions of a cylindrical channel, and also the effects of plasma generated at the walls as the aluminum is ablated. As a result, the beam will decompose over the dispersive waveguide modes, and this will affect the transverse coherence of the beam as it propagates, ultimately limiting the maximum depth that laser-etching can reach.

To measure transverse beam coherence, we use a Youngs two-slit interference setup. By measuring the fringe visibility for various slit separations, we can extract the transverse coherence as a function of displacement across the beam. However, this requires many data runs for different slit separations. Our solution to this problem is a novel approach to transverse coherence measurements: a modified Michelson interferometer. Flipping the beam left-right on one arm, we can interfere the beam with its own mirror-image and characterise the transverse coherence across the beam in a single shot.

Keywords: materials processing, ultrafast laser, pulsetrain-burst, laser micromachining, coherence, beamspread, interferometer

1. INTRODUCTION

It has been shown that lasers often confer special advantages in making tiny holes and vias. These tiny channels are used in many applications (interconnections between layers in used in the semiconductor industry, fabrication of microfluidics, fuel injectors, etc.). Ultrafast lasers do a particularly good job for many special materials or needs, particularly glasses, ceramics, fine processing of metals, and transparent biotissues. Among methods of ultrafast-laser processing, it has been shown that *pulsetrain-burst* processing, using a series of ultrafast laser pulses, at a repetition rate of 1 MHz or greater, is less likely to leave cracks or residual stress in the target material, and will instead typically result in an atomically smooth locally re-melted surface.

It is important to identify what factors determine the limits for hole-size and depth, for these lasers. A number of other experimenters have looked at this issue, considering, for example, the relation between hole

Send correspondence to: R.S. Marjoribanks, E-mail: marj@physics.utoronto.ca, Telephone: 416 978 6769
[c] current address: Universität Heidelberg, Seminarstr. 2, 69117 Heidelberg

Photonics North 2006, edited by Pierre Mathieu, Proc. of SPIE Vol. 6343, 63432A, (2006)
0277-786X/06/$15 · doi: 10.1117/12.707967

depth, fluence, number of pulses, pulse length, etc. Among these, measurements relating to drilling through soda-lime glass and leaded glass have been conducted;[2] for pulses at $\lambda = 845$ nm and 1064 nm, this work considered the relation between the depth of the drilled hole and the laser pulse duration, the relation between depth and the number of pulses accumulated, and the effect of ambient-air ionization on hole depth. The per-pulse depth, and other measurements on copper foil have also been investigated,[3] for pulses of duration 150 fs – 30.3 ps. Laser ablation has been studied for various metals (nickel, copper, molybdenum, indium, tungsten and gold) under irradiation by pulses of duration $\tau = 0.5$ ps and wavelength $\lambda = 248$ nm,[4] which work showed the effect of atmospheric pressure on drilling. It has been shown that channels of a few micrometers diameter, and over 1 mm deep may be drilled into quartz.[5] This was accomplished with a 790 nm wavelength laser and 100 – 200 fs pulses. It was found that the channel depth was determined by the laser fluence, and the number of laser shots. The relation between depth per pulse and pulse energy and duration has also been investigated,[6] over a wide range of pulse durations.

In this article, we report on drilling with an ultrahigh repetition rate (133 MHz) laser delivering *pulsetrain-bursts* of $3 - 15$ μs duration, comprising series of 10 – 10,000 pulses, and energies up to 15 mJ per burst, with individual pulse durations of 1 ps and individual pulse energies up to 10 μJ. It has been seen to drill clean, low-residual-stress holes in fused silica without leaving inbuilt stresses or causing fracturing,[7,8] and to produce deep smooth low-debris holes in aluminum.[9]

The pulsetrain-burst delivery has been seen to rapidly drill deep uniform holes in glass and metals, and several effects previously identified as the cause of hole-depth saturation in ultrafast-laser hole-drilling (such as energy attenuation in the sidewalls, and interaction with in-channel plasma) likely apply here. But — for both low- and high-repetition-rate laser micromachining — little is known about the *optical physics, per se,* of pulse propagation down drilled channels, and especially channels which may have some plasma still inside. For ultrafast-laser pulses, particularly, pulse dispersion and loss of optical coherence may play a significant role in changing the etch rate of laser micromachining.

A scenario like this can be imagined: After the channel has been well-established, and the beam continues to propagate through it, reduced energy continues to be absorbed in the side-walls, or else they will continue to etch back. Initially, the beam has a gaussian intensity distribution, and once the hole has been drilled to some depth, this clips the beam, and then for the transmitted portion it acts as a cylindrical waveguide. A gaussian beam is not a mode of such a waveguide, for which normal modes are Bessel functions. So when a gaussian beam enters the hole, it decomposes over the Bessel function modes. Typical of waveguide modes, these are dispersive, and travel with different phase speeds, so dispersion of the beam will result, phase-fronts will become complex across the pulse-front, and large fluctuations of the intensity can appear, much like caustics of a ray-trace picture. This dispersion and scattering may be studied optically.

For this present work, we drilled a series of increasing thicknesses of foil, and used them to interpret the progress of the ultrafast pulses through different depths of a single channel. We recorded the size of the beam as it exits the hole at the rear of the foil, measured the far-field beamspread, and characterized the transverse coherence of the beam at the exit-hole, all of which we could use to characterize the optical evolution of the beam. Immediately as a hole is drilled, there will be plasma on the inside walls of the hole from the ablated aluminum, and pulses transmitted within will be further affected by 'soft' boundary conditions, as the complex-valued index of refraction follows the plasma density. In this case the normal modes will not be Bessel functions, but something more complicated again.

2. EXPERIMENTAL SETUP

The laser used in these experiments is a flashlamp-pumped picosecond Nd:glass system ($\lambda = 1054$ nm) purpose-built at the University of Toronto.[1] An oscillator with active-passive and feedback-controlled modelocking produces a quasi-cw pulsetrain of over 3000 pulses, with pulse duration $1.2 - 10$ ps (Figure 1). At the oscillator, pulses are created with energies of up to 1 μJ, and separated by 7.5 ns (133 MHz pulse frequency). A Pockels cell N-pulse slicer selects a square burst of pulses from the train, $0.05 - 10$ μs long, for further amplification (Figure 1). Two Nd:glass amplifiers increase the per pulse energy to up to $\sim 10\mu$J/pulse at the target, giving a total train energy of up to 12 mJ in a 10 μs burst. The oscillator is part of a Terawatt chirped pulse amplification (CPA) system, not used in this work.

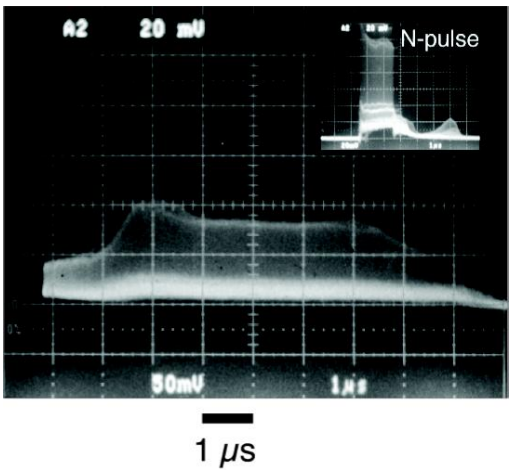

Figure 1. Oscilloscope trace of the pulsetrain-burst ultrafast-laser output: $10 - 3000$ nearly equal-intensity pulses, $1.2 - 10$ ps each, 7.5 ns between pulses (133 MHz); up to 10 μJ/pulse, 15 mJ/pulsetrain-burst. An N-pulse Pockels-cell slicer controls duration of the burst (inset).

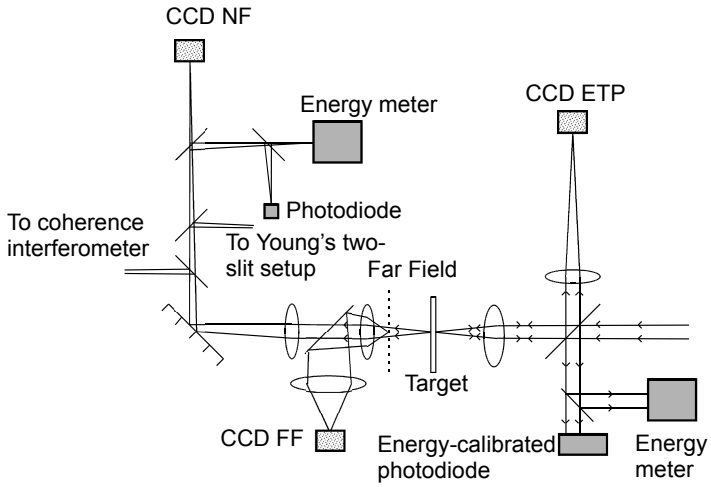

Figure 2. Schematic of equivalent target-plane (ETP), near field (NF), and far field (FF) imaging. The image of the exit-hole of the foil is relayed to the double slit of the Young's apparatus (see Fig. 3), and also to the CCD plane of the coherence interferometer (Fig. 5). incident- and transmitted-energy and pulsetrain are also recorded.

For the current experiment, the beam was focussed using a 13.8 mm focal-length lens. Focal spot imaging showed elliptical focal spots of size $4.7\mu m \times 7.1\mu$m. The aluminum target was mounted on an xyz translation stage of micrometer precision. Temporal profiles and total energies of the pulsetrains were measured for incident and transmitted beams. The incident beam was focused on the front of the aluminum foil. The focus was regularly monitored by autocollimating the retro-reflected beam, from which an equivalent-target-plane (ETP) image was recorded on each shot (Figure 2). A near field (NF) image of the back of the aluminum foil was recorded on each shot. After-target beamspread was measured using a far-field image of a plane 25 mm after the target.

All shots were performed in air with the laser at normal incidence to the target.

3. TRANSVERSE COHERENCE MEASUREMENT METHODS

3.1. Young's two-slit apparatus

Transverse coherence is typically measured using Young's two slit apparatus.[10] This method measures the coherence of one part of the image against another by interfering portions of the beam with each other. The sections of the image being combined are determined by the position of the slits, and so the separation of source-points being brought into interference is the separation of the slits. Therefore, to measure the transverse coherence length requires measurements of fringe visibility using several slits at different separation distances. This process requires data from many shots, and results in finding the coherence length by combining measurements from numerous drilling events, which themselves may exhibit significant variation.

For this experiment, we use a standard Young's two-slit setup (Figure 3). The back side of the aluminum foil (*i.e.*, the exit of the hole being drilled) is imaged onto the slits, and so the resulting interference pattern gives the transverse coherence of the beam at the exit of the hole. A focussed image of the transmission intensity of the slits (CCD-SB) was regularly monitored for each shot as well to make certain that the image was properly centered on the slits, and that the source intensities were well-balanced.

For each shot, an image of the interference pattern was obtained (Figure 4). The coherence may be obtained from the fringe visibility in these images, however if the intensity in both slits are not equal (this may occur if

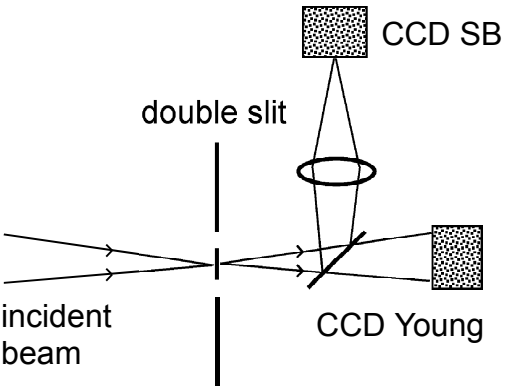

Figure 3. Schematic of the Young's two-slit setup used in this experiment. An image of the exit-hole beam-profile is relayed onto the slit-pairs, from which an interference pattern is recorded (CCD Young). At the same time, an image of the intensity transmitted through each slit is relayed to a slit-balance camera (CCD SB).

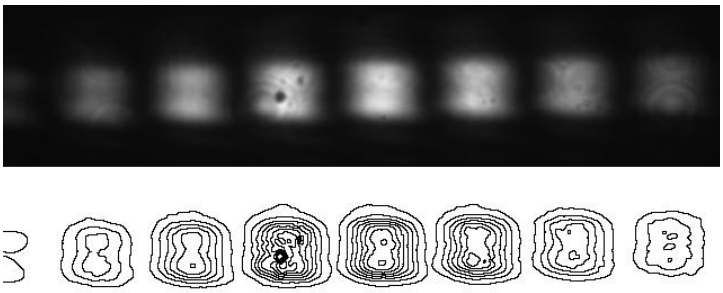

Figure 4. Sample image of interference pattern from the two-slit apparatus; greyscale (top) and contour plot (bottom). This particular shot shows the coherence of a pulsetrain-burst drilling through 150 μm of aluminum. The slits were 81 μm apart.

the hole is not perfectly centered on the beam) then the fringe visibility may be artificially low. To minimize this effect, the horizontal line which shows best fringe visibility was used for each such image.

One disadvantage of using the Young's two-slit setup is that, for each shot, the transverse coherence corresponding to only *one* fixed source-separation is measured. Therefore to find the transverse coherence length from the drop-off of fringe visibility, as source points are increasingly separated, many experimental runs must be performed. Another disadvantage is that the image for which the coherence is measured is necessarily out of focus. The fringes are only visible at a plane beyond the slits, and the coherence of the image focussed at the slits is being measured. So if the slits are vertical, then any features in the beam in the vertical direction will be defocussed at the plane at which the fringes are measured. Finally, in an experiment such as this, where the coherence is being measured at the end of a channel that it drills, it is often the case that the center of the image of the beam (or the channel) shifts slightly from shot to shot. In this case, the intensity on each slit will be different, and this will artificially decrease the fringe visibility. For small departures from perfect balance, the reference of the slit-balance camera (CCD SB) can in principle be used to correct the fringe-visibility.

3.2. Coherence interferometer

Using a modified Michelson interferometer setup the transverse coherence corresponding to all slit widths is measured in one shot. This is done by interfering one image of the back of the hole with its own mirror image. The resulting image shows the interference pattern between any distance to the right of the center with that same distance to the left of the center. So using this image, the transverse coherence may be found for any transverse separation.

This setup uses two different images which both image the back of the aluminum hole: COH and COH-REF. On COH, both images are made to overlap completely to determine the coherence. On COH-REF, they are kept separate and monitored on each shot to ensure that the beams stay in the same relative position, and that the intensity distribution of each is separately known.

Since one arm of the interferometer has only one mirror (1), and the other arm has two mirrors (2,3) the left and right sides of one beam are flipped relative to the other (Figure 5). The incident beam first passes through a linear polarizer. This is to ensure that if either of the beam splitters (or other optical elements) treat perpendicular polarizations differently, this will not artificially reduce the interference. The variable neutral-density filter in the upper arm ensures that the intensity of both beams are equal; they would not otherwise be equal since the other beam goes through one more beam-splitter on the way to CCD COH.

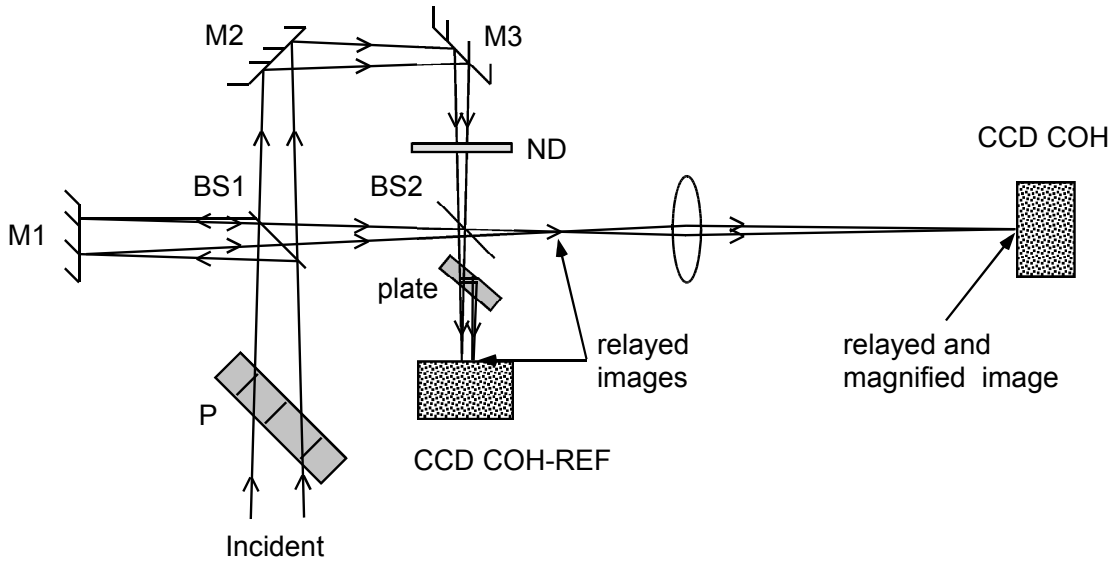

Figure 5. Schematic of the modified Michelson interferometer used to measure transverse coherence. The recorded interference pattern is formed (CCD COH) from two images (one flipped horizontally) of the exit hole of the channel through the aluminum foil, the same image as relayed to the near-field camera in Fig. 2(CCD NF). A second camera (CCD COH-REF) records the separate beam profiles, as a reference.

To get measurable fringes, it is necessary to make both beams focus at the same point, but at a small vertical angle between them. This is accomplished by setting mirror M3 and beam-splitter BS2 to non-zero vertical angles such that the beams intersect at the focus. This produces an image with horizontal fringes (Figure 6). The image obtained on COH-REF is obtained by shifting one beam horizontally with respect to the other. This is done partially by alignment, and partially through the use of a glass plate, set at an angle to the beam, to increase image walk-off (Figure 7).

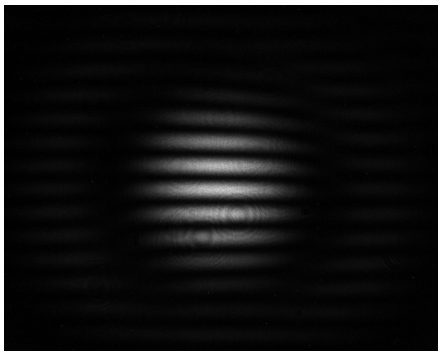

Figure 6. Sample image from the interferometer camera (CCD COH). This shows an image of the exit-hole beam-profile interfering with its left-right mirror-image, at a small vertical angle to produce horizontal fringes.

Figure 7. Sample image from the interferometer reference camera (CCD COH-REF). This separately shows each image (original and flipped) of a beam after having drilled through 50 μm of aluminum. The slight asymmetry in the image of the hole emphasizes that one beam is a faithful mirror image of the other. The difference in intensities is a result of the glass plate in one beam.

For the experimental setup, the image produced on CCD NF (magnification $\sim 40\times$) occupies only a small fraction of the area of the CCD, so the distance between adjacent fringes would be about 8 pixels on the CCD.

To improve the resolution, a lens is used (Figure 5) to relay the image again with magnification. For the setup used in this experiment, the additional magnification factor was measured to be 10×.

Consider the intensity profile along a vertical line through the COH image, at some distance displaced from the centerline of the spot: the mutual coherence of two sources at a separation corresponding to *twice* that distance (displaced an amount left against an equal amount right) may be calculated from the fringe visibility. Proceeding in this way throughout the width of the COH image, the fringe visibility may be measured as a function of transverse distance.

3.3. Comparison of results

For this method to prove to be valid, it must be shown to give the same result as a Young's two-slit apparatus, or differences between the results must be explained in terms of known issues with the two-slit approach. To compare these measurements, several data-points were collected using each method. For this, pulses late in the train, transmitted after having drilled through 150 μm of aluminum were used. Several samples of data from this experiment are plotted in Fig. 8. Each two-slit data-point corresponds to a different shot, and each interferometer curve corresponds to a different shot.

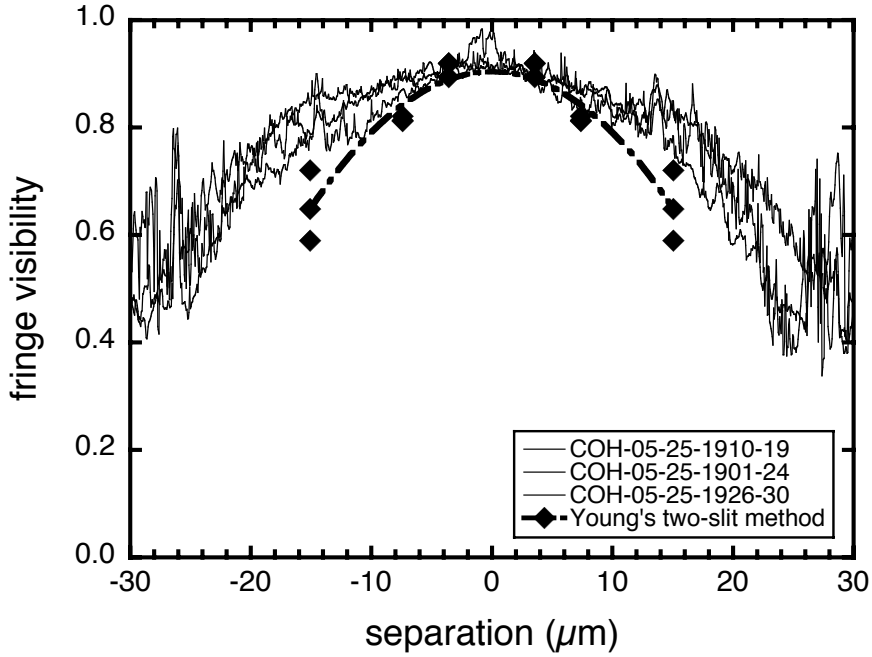

Figure 8. Plots of transverse coherence as obtained from the interferometer, along with coherence datapoints obtained from the two-slit setup at several slit separations.

This data shows reasonable agreement between the data taken from the interferometer and that from the two-slit setup. The data from the interferometer varies from shot to shot, but this variation is approximately the same as that in the two-slit data. This is consistent with the observation that each shot produces a slightly different exit hole, and near-field pattern. Although each method shows a decrease in coherence with source-separation, the coherence measured with the two-slit is lower at each separation.

This is likely a limitation of the two-slit approach. It has been observed that because of the shot-to-shot beam variation, the intensity transmitted by each slit (measured using the CCD SB) varies by as much as 30%.

By using the best fringe visibility, as found from different horizontal lineouts at different vertical heights, it is often possible to partially compensate for this problem. However, since the image is defocussed and blurred-out vertically, regions of poor slit-balance (one slit illuminated more than the other) will blend with regions of good slit-balance along the vertical direction. This will artificially and irrecoverably reduce the coherence as measured with the two-slit setup. This effect is likely responsible for the lower fringe visibility seen using the two-slit setup.

Since the interferometer uses two beams which produce an image in the same plane (this is necessary to produce interference fringes), this problem does not exist using the flipped-interferometer setup.

4. OPTICAL PHYSICS EFFECTS, IN HOLE-DEPTH SATURATION

The purpose of this experiment, after testing the modified Michelson interferometer, was to test the manner in which a Gaussian beam drills through a foil of metal. To do this, identical data sets were gathered for three aluminum foil (Goodfellow Corporation) thicknesses: $50, 100, 150$ μm. In each case, the target and lens positions (Figure 2) were set such that the incident beam was focussed on the front surface of the foil, and the after-target optics (interferometer, near field, etc.) precisely imaged the back surface of the foil. Using this procedure, it was possible to calculate the coherence loss and dispersion as the beam propagates down the channel.

Additionally, for each foil thickness, several data runs were taken, corresponding to different source separations (for the two-slit setup). This was used to confirm that the two-slit method and the modified Michelson interferometer methods produced equivalent results, as shown above.

We used the near-field camera (CCD NF) to monitor the exit-hole intensity distribution (Figure 9). This is important in determining both the shape of the beam exiting the hole, and the position of the hole itself. After the laser is aligned, only the target is moved, to fresh sites, but the position of the exit-hole is found to vary from shot to shot nonetheless. If the near-field shows an off-center shot, it is likely that the coherence will be difficult to measure on either measurement setup. Ideally, even if the near-field is uneven in intensity, the coherence measurements will still work (just by comparing points of equal intensity). However, if the intensity distribution is too asymmetric, left-right, it becomes significantly more difficult to find points of equal intensity.

Figure 9. Sample near-field image of the back surface of a 150 μm aluminum sheet on burnthrough

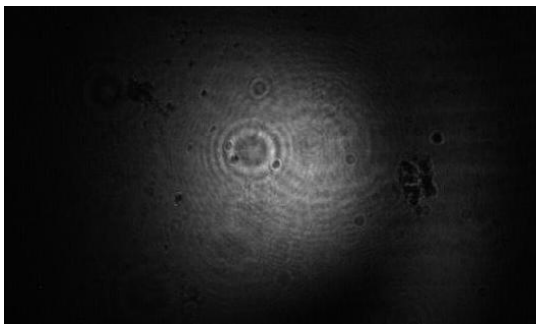

Figure 10. Sample image from far-field CCD. This shows the image of a beam 25 mm after burning through 100 μm of aluminum

We measure the far-field beamspread (divergence angle) after the target using the far-field camera (CCD FF). Based on the size of the spot on the far-field object plane (Figure 10), and the 25mm distance between the hole and this plane, it is simple to calculate the beamspread angle. This angle is later used in determining characteristics of the beam as it exits the hole. We use the equivalent target plane image (ETP) to align the target and targeting lens. Whenever the front surface of the target is at the focus, the retro-reflected beam will be auto-collimated back through the target lens, and this is used to determine the ideal target position. This is monitored on each burnthrough shot to make certain that the target remains at the beam-waist. The photodiodes (one before the target, one after) are used to monitor the pulsetrain-envelope from shot to shot. They are also used to determine the number of pulses for the beam to burn through the target, to determine the etch-rate.

5. HOLE DEPTH, TRANSVERSE COHERENCE, AND BEAMSPREAD

The intensity envelopes from the photodiodes were used to determine the time at which the passage etched through the foil is complete. These values were determined for several foil thicknesses, and it was assumed that the etch rate at a certain depth into the foil depends on that depth, regardless of the ultimate thickness of the foil. From this, the differential etch rate through the foil was deduced (Fig. 11).

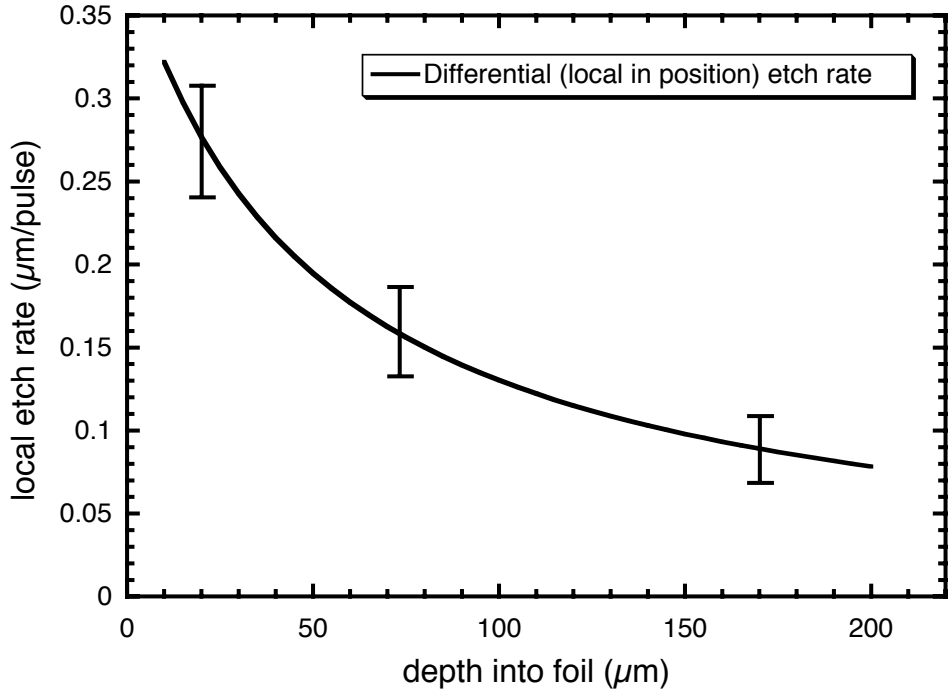

Figure 11. Etch rate as determined from burnthrough times: the number of pulses to drill through each of a series of foil thicknesses was measured; assuming the first half of a $50\mu m$ is etched much like a $25\mu m$ is etched, a picture of the differential etch-rate for different depths of drilling can be built up.

Using the modified interferometer, the transverse coherence was measured for $50, 100, 150$ μm foil thicknesses (Figure 12). The data was taken over several shots, and averaged where appropriate. For thinner foils, the hole diameter (as measured on the near-field) is small, so the transverse coherence data is confined to a smaller range. For all foil widths, and for no foil, the transverse coherence at zero distance peaks at just under 1, and for an unobstructed beam, it remains nearly constant at 1 across the spot diameter, consistent with a coherent laser beam. For each foil thickness, the transverse coherence drops off with increasing thickness. Each of these coherence curves has a well-defined peak and curvature, and it is therefore possible to determine the width (FWHM), which is taken as the transverse coherence length. It is clear from this plot that the transverse coherence drops off with increasing depth of hole drilled. The far-field beamspread was also recorded, and averaged for each foil thickness. This is used for calculations in the analysis.

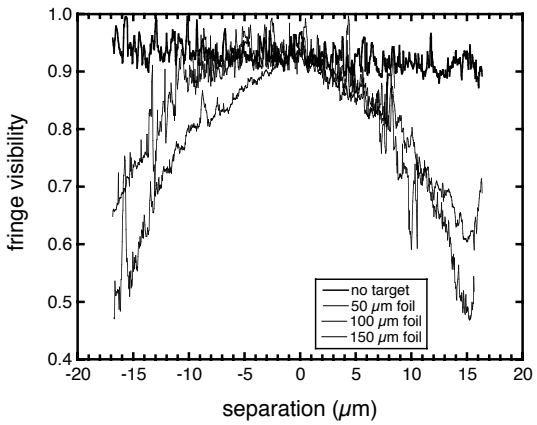

Figure 12. Plots of transverse coherence as obtained from the interferometer for all three foil thicknesses. Included for reference is a plot of transverse coherence for an unobstructed laser beam at a point 150 μm beyond the beam-waist.

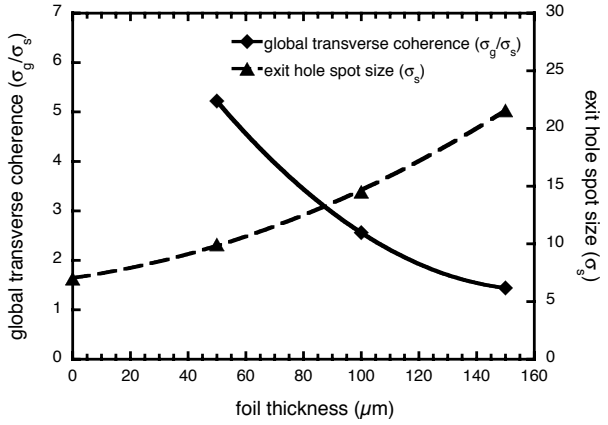

Figure 13. The global coherence decreases with depth of drilling, while at the same time the diameter of the exiting beam increases; in this range of foil thicknesses, the second is more important, and the far-field divergence angle *decreases* with increasing foil thickness. At thicknesses above 150m there is evidence that the coherence-loss begins to dominate, as global coherence drops to unity.

6. ANALYSIS OF DATA: THE GAUSSIAN SCHELL MODEL

6.1. Gaussian Schell model sources

A planar and secondary source generating Gaussian Schell-model beams is a beam which displays Gaussian distributions of both the optical intensity and the degree of transverse coherence.[11,12] The degree of spatial coherence measures the correlations between the amplitudes of the optical field at two points across the beam and it is the normalized form of the transverse spatial coherence function, more precisely the cross-spectral density function. Schell-model sources are characterized by the property that their spectral degree of coherence in the source plane depends only on the difference $(r1 - r2)$, so it is independent of the absolute positions where it is measured. This validates the methods used to calculate fringe visibility from the interferometer image; the best fringe visibility is used regardless of where on the beam it occurs. The optical intensity and the degree of spatial coherence for a monochromatic wave field are thus given by the expressions

$$S(\rho, z) = S_0 \exp\left[-\frac{\rho^2}{2\sigma_S^2 \Delta^2}\right]$$

and

$$\mu(\rho_1, \rho_2, z) = \exp\left[-\frac{(\rho_2 - \rho_1)^2}{2\sigma_g^2 \Delta^2}\right] \exp\left[\frac{ik(\rho_2^2 - \rho_1^2)}{2R}\right] \tag{1}$$

where Δ is the beam expansion coefficient (this is 1 at the beam-waist) and R is the radius of wave-front curvature which are constants for a given observation plane. The beam radius is $\sqrt{2}\sigma_S\Delta$ and its correlation width is $\sqrt{2}\sigma_g\Delta$.

According to the Gaussian-Schell model, for a beam satisfying the source properties, there is a relationship between the beam-waist size, the beam-waist coherence, and the far-field divergence. These equations are similar to the standard Gaussian beam propagation formulae, with corrections relating to imperfect transverse coherence:

$$\rho(z) = \sqrt{2}\sqrt{2\sigma_S^2 + \frac{2z^2}{k^2}\left[\frac{1}{(2\sigma_S)^2} + \frac{1}{\sigma_g^2}\right]} \tag{2}$$

angular spread of the beam:

$$\theta(z) = \frac{\sqrt{2}}{k}\sqrt{\frac{1}{(2\sigma_S)^2} + \frac{1}{\sigma_g^2}} \tag{3}$$

NB: The beam radius, $\rho(z)$, is defined as the value of radial distance ρ for which the intensity drops to $1/e^2$ of its maximal value.

6.2. Applying the Gaussian Schell model

As the beam exits the newly formed channel, it may be considered as a Gaussian-Schell source. This is however an approximation. The near-field image, which is the back of the hole, is never a perfect gaussian, and often shows irregular features (Figure 9). Since the far-field and near-field sizes are measured, and the coherence distances are deduced, the validity of the model can be tested by comparing the measured far-field size with that calculated based on the Gaussian-Schell model using the near-field size and coherence widths (Figure 14).

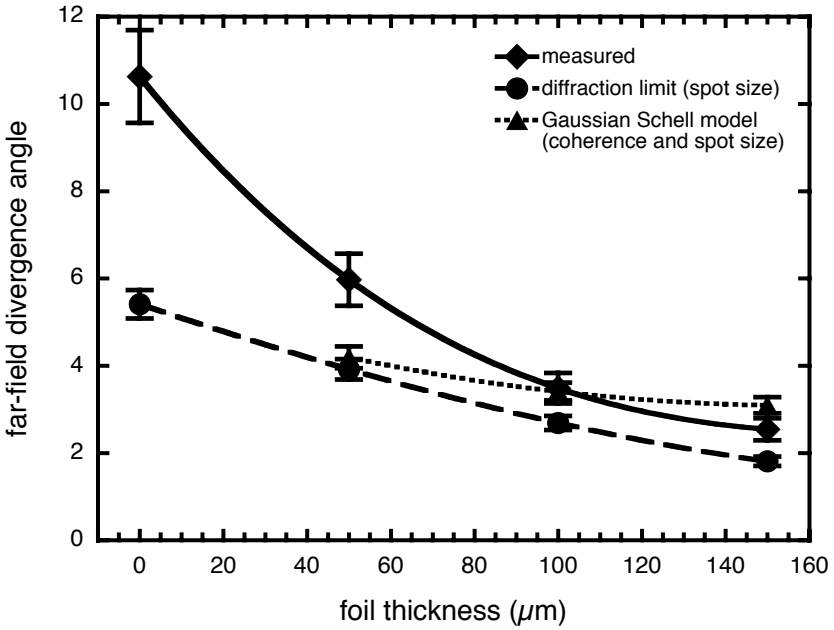

Figure 14. The far-field spot size. This is measured on the far-field CCD. It is also calculated based on known coherence widths and near-field spot size. Finally it is calculated based on a diffraction-limited (perfect coherence) beam

This shows that the far-field angle actually decreases with foil-width even though coherence width decreases as well. This is normally unexpected, since a randomization of phases throughout the beam (loss of coherence) should result in increased far-field divergence. However, the near-field spot size also increases (larger-diameter intensity profile at the exit-hole) with increased foil thickness. Using the gaussian beam propagation formula, an increased beam-waist size allows for a decreased far-field spot size. Thus, essentially, propagation down the drilled channel allows a beam transformation like a beam-expander telescope.

Without a foil, the natural far-field spot size is substantially larger than the estimated diffraction limit. This would be consistent with an M^2 of approximately 2 for our laser. As the foil thickness becomes larger, the far-field spot size approaches the diffraction limit. This suggests that the channel also acts as a spatial filter for the beam, at the same time that propagation causes disruption in the transverse coherence and expands the beam.

7. CONCLUSIONS

The first portion of this experiment was the design and testing of a new method of transverse coherence measurement. First we used a traditional method of coherence measurement: the Young's two-slit setup. Since this method only gives the coherence at one distance per measurement, we used a modified Michelson interferometer. By flipping one beam left-right relative to the other, one image could be used to determine the transverse coherence at all points across the beam. Using the two-slit setup, we measured the transverse coherence of the beam after drilling through a sheet of aluminum foil. This data was compared to the that obtained under the same circumstances with the new interferometer setup. It was found that the two methods show approximately the same patterns in transverse coherence.

Using this new setup, we attempted to find the relationship between coherence loss and beamspread as a laser beam propagates through a newly formed channel in an aluminum sheet. As the beam propagates down the channel, the new boundary conditions cause the gaussian beam to decompose into normal modes (Bessel functions), measurable in terms of transverse coherence loss across the beam.

The expected coherence loss was measured, along with a decreasing etch-rate. As the foil thickness was increased, the transverse coherence length and etch-rate dropped off. This is consistent with the idea that loss of laser-coherence is related to drill depth saturation. This was then compared to the Gaussian Schell model, approximating the exit-hole of the channel to be the source. The far-field angle was found to decrease with increasing foil-width, approaching the diffraction-limited size.

The overall picture of pulsetrain-burst drilling, then, is one in which non-normal mode propagation of a free-space gaussian beam in a cylindrical waveguide, with plasma at the walls, leads to a disturbance of the phase fronts due to dispersion and to scattering at the walls. The increasing loss of coherence causes the beam to spread, though as the beam continues to cut its own channel it provides its own spatial filter. The loss of coherence and scattering leads to higher loss of energy than compared to free-space expansion clipped at the hole's diameter. The increasing hole-diameter and simultaneous spatial filtering leads to a smooth expanded beam, which also decreases the on-axis intensity. These effects, together, result in hole-depth saturation at a depth smaller than that expected for simple free-space gaussian drop-off of intensity, with absorption at the side-walls.

8. ACKNOWLEDGEMENTS

The authors acknowledge support from the Canadian Institute for Photonic Innovations, the Centre for Photonics of Ontario Centres of Excellence, Inc., and the Natural Sciences and Engineering Research Council of Canada.

REFERENCES

1. R. S. Marjoribanks, F. W. Budnik, L. Zhao, G. Kulcsar, M. Stanier, and J. Mihaychuk, "High-contrast terawatt chirped-pulse-amplification laser that uses a 1-ps Nd:glass oscillator," Opt. Lett. **18**, 361- (1993)
2. Shah, L., Tawney, J., Richardson, M., Richardson, K., Appl. Surf. Sci. 2001 pp. 151
3. S. Nolte, C. Momma, H. Jacobs, A. Tunnermann, B. N. Chichkov, B. Wellegehausen, and H. Welling, J. Opt. Soc. Am. B 14, 2716 (1997).
4. S. Preuss, A. Demchuk, and M. Stuke, Appl. Phys. A 61, 33 (1995).
5. H. Varel, D. Ashkenasi, A. Rosenfeld, M. Wahmer, E. E. B. Campbell, Appl. Phys. A 65, 367 (1997).
6. C. Momma, B.N. Chichkov, S. Nolte, F. von Alvensleben, A. Tunnermann, and H. Welling, Opt. Commun. 129, 134 (1996).
7. P. R. Herman, A. Oettl, K. P. Chen, and R. S. Marjoribanks in Commercial and Biomedical Applications of Ultrafast Lasers, Proc. SPIE 3616, pp. 148155, 1999.
8. L. McKinney, F. Frank, D. Graper, J. Dean, P. Forrester, M. Rioblanc, M. Nantel and R.S. Marjoribanks Proc. SPIE Vol. 5970, 59701L, 2005.
9. M. Lapczyna, K. Chen, P. R. Herman, H. W. Tan, and R. S. Marjoribanks Appl. Phys. A69 (Suppl), pp. S883886, 1999.

10. B. J. Thompson and E. Wolf, "Two-beam interference with partially coherent light," J. Opt. Soc. Am. 47, 895- (1957)
11. E. Wolf and E. Collett, "Partially Coherent Sources which Produce the same Far-Field Intensity Distribution as a Laser" Optics Communication. June 1978, pp. 293
12. Ari T. Friberg, Taco D. Visser, Emil Wolf, "A Reciprocity Inequality for Gaussian Schell model beams and some of its consequences", Optics letters, March 15 2000, pp. 366